Editors' Suggestion

1D Magneto-Optical Trap of Polyatomic Molecules

Louis Baum,[1,2,*] Nathaniel B. Vilas,[1,2] Christian Hallas,[1,2] Benjamin L. Augenbraun,[1,2] Shivam Raval,[1,2] Debayan Mitra,[1,2] and John M. Doyle[1,2]

[1]Harvard-MIT Center for Ultracold Atoms, Cambridge, Massachusetts 02138, USA
[2]Department of Physics, Harvard University, Cambridge, Massachusetts 02138, USA

(Received 29 January 2020; accepted 9 March 2020; published 31 March 2020)

We demonstrate a 1D magneto-optical trap of the polar free radical calcium monohydroxide (CaOH). A quasiclosed cycling transition is established to scatter $\sim 10^3$ photons per molecule, predominantly limited by interaction time. This enables radiative laser cooling of CaOH while compressing the molecular beam, leading to a significant increase in on axis beam brightness and reduction in temperature from 8.4 to 1.4 mK.

DOI: 10.1103/PhysRevLett.124.133201

Laser cooling and evaporative cooling are key tools of atomic, molecular, and optical physics that are used to produce ultracold atomic and molecular samples [1,2]. Ultracold atoms have enabled the study of degenerate quantum gases [3], high-precision clocks [4], quantum many-body physics, and quantum simulation of condensed matter systems [5]. Polar molecules, with their additional internal degrees of freedom and long-range interactions, promise further access to novel phenomena in the ultracold regime [6]. For example, diatomic molecules have been identified for applications that include precise searches for physics beyond the standard model [7–10], quantum simulation [11–13], studies of fundamental collisional [14] and chemical [15–17] processes, and production of exotic ultracold atoms through photodissociation of ultracold molecules [18,19]. While diatomic molecules are a rich resource (and are only beginning to be explored), polyatomic molecules have qualitatively distinct advantages at the frontier of quantum science. Ultracold polyatomic molecules have been identified for applications including improved precision searches for the electron electric dipole moment (EDM) [20] and for dark matter [21], novel quantum computation [22–24] and quantum simulation platforms [25,26], the control of the primordial chemical reactions that gave rise to life [27], the study of biomolecular chirality [28,29], and the study of ultracold collisions and quantum chemistry in increasingly complex systems, while maintaining single quantum state control [30,31].

With such promise, there have been intense efforts to cool molecules. "Indirect" approaches, such as association techniques, like coherent adiabatic binding of laser-cooled atoms, have led to a variety of ultracold diatomic bialkali samples including a quantum degenerate Fermi gas of KRb [32,33]. "Direct" cooling approaches use electromagnetic fields (e.g., lasers or pulsed external fields) to slow and cool molecules [34–42]. These techniques include Sisyphus-type approaches, which have, for example, produced samples of H_2CO as cold as 420 μK [43,44]. Laser cooling has been identified as being potentially applicable to a variety of molecular structures [6,45–51], including polyatomic species composed of a single metal atom bound to an electronegative radical, called "MOR" molecules [52–54]. Crucially, laser cooling offers a path to trapped μK samples of molecules in single internal and motional quantum states. SrF [41,55–60], CaF [42,61–66], and YO [67–69] have all been laser cooled and loaded into magneto-optical traps (MOTs). SrF and CaF have been cooled below the Doppler limit and transferred to optical or magnetic traps [70–72]. Sisyphus laser cooling of the polyatomic molecules SrOH and YbOH has been achieved [73,74], and coherent optical forces have been applied to SrOH [75].

In this Letter, we demonstrate radio frequency (rf) magneto-optical (MO) cooling and compression (1D MOT) of a beam of the polyatomic molecule $^{40}Ca^{16}OH$, an archetypal example of the broader class of MOR molecules. In doing so, we realize a cycling scheme capable of scattering $\sim 10^3$ photons. We characterize the MO forces applied here by extracting force constants and damping rates. A concomitant on axis increase in molecular density is observed. This demonstration of MO cooling establishes a route towards deep laser cooling and optical trapping for numerous species of polyatomic molecules.

Effective MO cooling and compression requires scattering many photons without losing population to states that do not couple to the laser light ("dark states"). Establishing such a cycling transition in molecules requires closing both vibrational and rotational degrees of freedom, as depicted in Fig. 1. Vibrational decay is not governed by rigorous selection rules but instead by wave function overlap, which is quantified by Franck-Condon factors (FCFs). CaOH is an example of a broad class of polyatomic molecules that have been identified as promising candidates for laser cooling due to their diagonal FCFs and strong electronic transitions

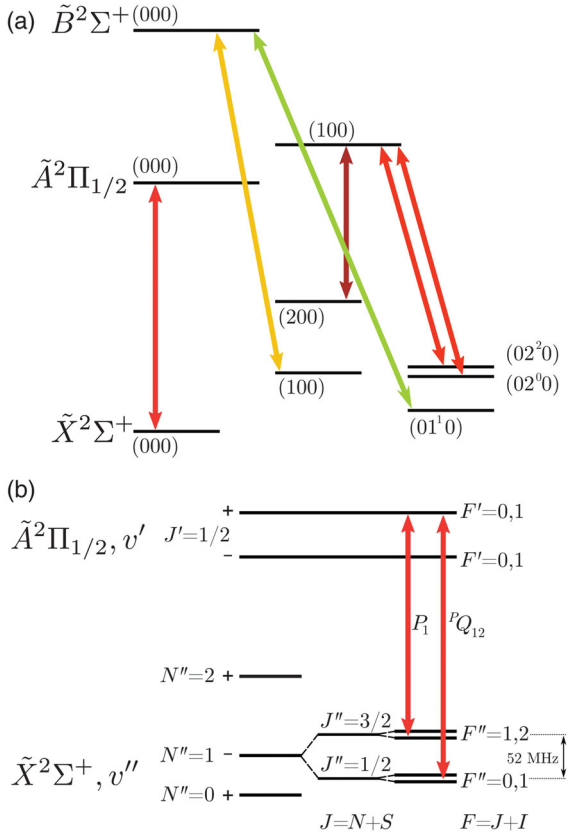

FIG. 1. (a) Laser cooling scheme for CaOH. The vibrational structure depicted here indicates all levels that are addressed with lasers in order to limit the branching ratio to other vibrational states to 4.5×10^{-4}. (b) Rotational structure of CaOH illustrating the 52 MHz spin-rotation splitting in the electronic ground state as well as the unresolved hyperfine structure (1.5 MHz and 7 kHz in the $J''=\frac{3}{2}$ and $J''=\frac{1}{2}$ states, respectively [79]). The $\tilde{X}^2\Sigma^+(v_1''v_2''v_3'') \rightarrow \tilde{A}^2\Pi_{1/2}(v_1'v_2'v_3')$ $P_1(J''=\frac{3}{2})$ and $^PQ_{12}(J''=\frac{1}{2})$ rotationally closed transitions are shown [46]. The parity of the ground states is indicated by the sign to the right of the N'' value while the parity of the excited states is indicated to the right of the J' value. The rotational structure of the $\tilde{B}^2\Sigma^+(000)$ state is analogous to that of the $\tilde{X}^2\Sigma^+$ states and is not pictured. Rotational closure on repumping lines through this state is achieved by driving $P_1(J''=\frac{3}{2})$ and $^PQ_{12}(J''=\frac{1}{2})$ transitions to the $\tilde{B}^2\Sigma^+(N'=0, J'=\frac{1}{2}, +)$ state. The level diagrams are not to scale.

[52,76]. The main laser cooling transition in CaOH is the $\tilde{X}^2\Sigma^+(000) \rightarrow \tilde{A}^2\Pi_{1/2}(000)$ transition with a natural linewidth of $2\pi \times 6.4$ MHz at 626 nm [77]. The highly diagonal FCFs of the $\tilde{A}^2\Pi_{1/2}(000)$ state suppress spontaneous decay to higher vibrational states during a single scattering event; nonetheless, significant optical pumping into excited vibrational states can occur when many photons are scattered. CaOH has three vibrational modes: a symmetric stretch, a doubly degenerate bend, and an antisymmetric stretch. These vibrational modes are labeled with four quantum numbers $(v_1, v_2{}^l, v_3)$, where v_1, v_2, and v_3 indicate the number of quanta in the symmetric stretching mode, the bending mode, and the antisymmetric stretching mode, respectively. l labels the nuclear orbital angular momentum in the bending mode and takes values of $l = -v_2, -v_2+2, \ldots, v_2$ [78]. Five repumping lasers, listed in Table I, are used to establish a quasiclosed cycling scheme and recover population in these states, as depicted in Fig. 1. Branching ratios within this cycling scheme are reported in the Supplemental Material [82].

TABLE I. Optical transitions and corresponding wavelengths driven to form a quasiclosed cycling transition in CaOH. The $\tilde{X}^2\Sigma^+(000) \rightarrow \tilde{A}^2\Pi_{1/2}(000)$ transition is the main cooling line while the other five frequencies correspond to vibrational repumping lasers.

Transition	Wavelength (nm)
$\tilde{X}^2\Sigma^+(000) \rightarrow \tilde{A}^2\Pi_{1/2}(000)$	626.4
$\tilde{X}^2\Sigma^+(100) \rightarrow \tilde{B}^2\Sigma^+(000)$	574.3
$\tilde{X}^2\Sigma^+(200) \rightarrow \tilde{A}^2\Pi_{1/2}(100)$	650.4
$\tilde{X}^2\Sigma^+(02^00) \rightarrow \tilde{A}^2\Pi_{1/2}(100)$	629.0
$\tilde{X}^2\Sigma^+(02^20) \rightarrow \tilde{A}^2\Pi_{1/2}(100)$	630.0
$\tilde{X}^2\Sigma^+(01^10) \rightarrow \tilde{B}^2\Sigma^+(000)$	566.0

Notably, both the $\tilde{X}^2\Sigma^+(01^10)$ and $\tilde{X}^2\Sigma^+(02^20)$ states need to be repumped. Decays to these states are nominally forbidden by an approximate $\Delta l = 0$ selection rule that originates from the separation of electronic and vibrational degrees of freedom in the Born-Oppenheimer approximation. The breakdown of this selection rule has been observed previously for $\Delta l = 1$ transitions in CaOH (and other similar systems) and is attributed to a second order process involving Renner-Teller mixing and spin-orbit coupling leading to intensity borrowing via the $\tilde{B}^2\Sigma^+(01^10)$ state [76,80,81]. Decay to the $\tilde{X}^2\Sigma^+(02^20)$ state was previously unobserved. We attribute the magnitude of this decay to a similar mechanism that relies on the mixing of vibrational states within the $\tilde{A}^2\Pi_{1/2}$ manifold (see the Supplemental Material [82]). We measure the branching ratio out of this cycling scheme to be $4.5(7) \times 10^{-4}$, which is predicted to be dominated by decay to the $\tilde{X}^2\Sigma^+(12^00)$, $\tilde{X}^2\Sigma^+(12^20)$, and $\tilde{X}^2\Sigma^+(300)$ vibrational states. Details of this measurement will be the subject of a subsequent publication.

To avoid populating rotational dark states, each laser beam (main and all repumpers) contains two frequency components separated by the spin-rotation (SR) splitting of 52 MHz depicted in Fig. 1(b). The hyperfine splitting is below the natural linewidth of the main cooling transition and does not require additional frequency sidebands [79]. This type of transition ($J \rightarrow J' = J-1$) causes rapid optical pumping into magnetic dark states, significantly reducing the cooling and confining forces in molecular MOTs [83]. We address this by simultaneously switching

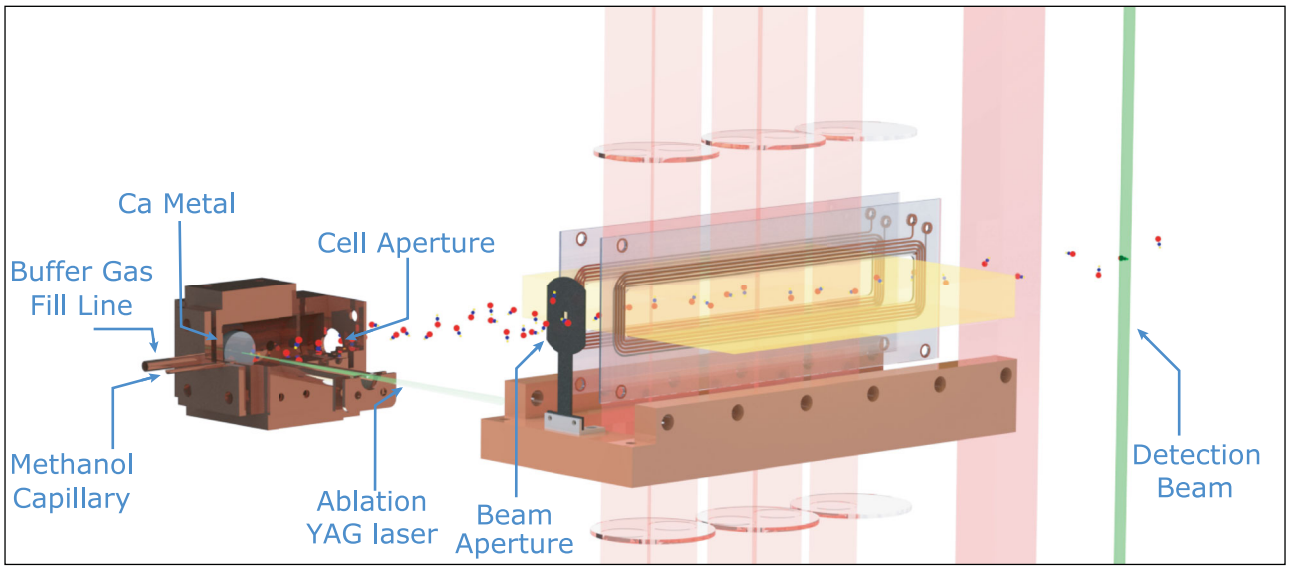

FIG. 2. A rendering of the experimental apparatus. On the far left is the two-stage buffer-gas beam source, depicted in a cut-away view for clarity: 35.5 cm from the exit of the buffer-gas cell, the molecular beam is collimated by a 3 mm square beam aperture, and, 39 cm from the cell, the molecules enter the interaction region where they are addressed with light from the main MO cooling beams in the vertical direction. Copropagating vertically are the (100), (200), and (02^00) repumping lasers indicated in red. The (02^20) and (01^10) repumping light, indicated in yellow, is multipassed in the horizontal direction and extends beyond the MO region. A separate vertically multipassed region containing (100) and (02^00) repumping light lies after the magnetic field coils and serves to recover population from excited vibrational states. Finally, the molecules encounter a detection beam of a smaller cross section than the cooling and repumping light, and the resulting laser-induced fluorescence is collected and imaged onto an EMCCD (electron multiplying charge coupled device).

both the laser polarization and the sign of the magnetic field gradient during cooling, which evolves magnetic dark states into bright states, as previously demonstrated in diatomic systems [59,62,67].

CaOH molecules are produced using a cryogenic buffer gas source [84,85] as depicted in Fig. 2. Hot calcium atoms are produced by laser ablation of a metallic calcium target inside of a copper cell held at ∼2 K while flowing six standard cubic centimeters per minute (SCCM) of helium buffer gas. We simultaneously flow a small amount (∼0.01 SCCM) of methanol vapor into the cell through a thermally isolated capillary at ∼250 K. Methanol molecules react with calcium atoms to produce CaOH. The CaOH molecules rapidly cool via collisions with the helium buffer gas. This produces CaOH at densities of $\sim 10^{10}$ cm^{-3} in a single rotational state, as measured by laser absorption in the cell. The cold CaOH molecules are entrained in the buffer gas flow and extracted from a two-stage cell into a cryogenic buffer-gas beam (CBGB) with a mean forward velocity of $v_f \sim 100$ m/s and a transverse velocity spread of $v_\perp \sim 20$ m/s [84]. The CBGB is collimated by a 3 mm square aperture located 35.5 cm from the exit of the buffer-gas cell, resulting in a transverse temperature $T_\perp \sim 8.4$ mK.

After exiting the aperture, the collimated molecular beam enters the interaction region containing six distinct wavelengths of light (main plus five repumpers). The combined laser light, with a beam diameter of 25 mm, makes five round trip passes through the interaction region as well as through a pair of $\lambda/4$ wave plates for 12.5 cm of total interaction length. The main laser cooling light is circularly polarized and retroreflected in a $\sigma^+ - \sigma^-$ configuration. Details are provided in the Supplemental Material [82]. The handedness of the polarization is rapidly switched using a voltage-variable wave plate (Pockels cell). A quadrupole magnetic field is generated with a pair of in-vacuum anti-Helmholtz coils and sinusoidally driven at the same frequency as the laser polarization switching with a controllable phase offset.

Following the interaction region, where MO cooling and compression take place, repumping lasers are applied to recover population from excited vibrational states. The molecules expand ballistically while propagating to the detection region, mapping the momentum distribution onto the spatial extent of the molecular beam. The molecules are then excited with lasers addressing the $\tilde{X}^2\Sigma^+(000) \rightarrow \tilde{B}^2\Sigma^+(000)$ and $\tilde{X}^2\Sigma^+(100) \rightarrow \tilde{B}^2\Sigma^+(000)$ lines with the resulting laser-induced fluorescence imaged onto an EMCCD camera. The collection efficiency of the imaging system is measured to be constant over the region occupied by the molecules. The resulting image is integrated along the direction of molecule propagation to produce a spatial beam profile, which we fit to a Gaussian distribution. We parameterize the width of the molecular beam by the standard deviation of the Gaussian fit. MO cooling and compression are seen as a narrowing of this width, as shown in Fig. 3. The main cooling laser intensity was

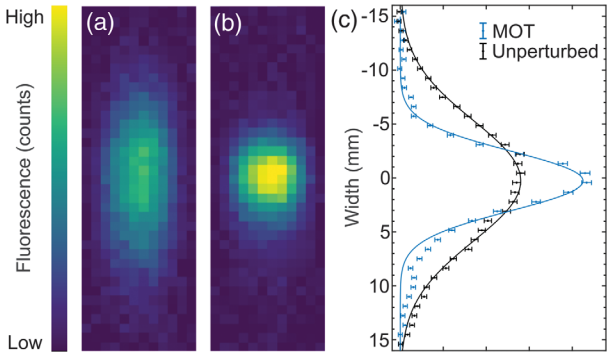

FIG. 3. Raw images of the molecular beam taken for (a) unperturbed CaOH molecules and (b) under 1D MOT conditions. The molecular beam propagates from left to right in these images, while the cooling and detection light propagates in the vertical direction. (c) Horizontally integrated molecular beam profiles indicating cooling and on axis density enhancement. Solid lines are fits to a Gaussian profile. These beam profiles have not been rescaled. The area of the MO compression trace is 78% of the unperturbed beam. Using the measured branching ratio out of our photon cycling scheme, this corresponds to ~550 photons scattered. At this laser intensity, on axis beam brightness is optimized. At higher intensities, we observe saturation of the cooling and compression effects, while the concomitant additional photon scattering leads to population loss to unaddressed vibrational states.

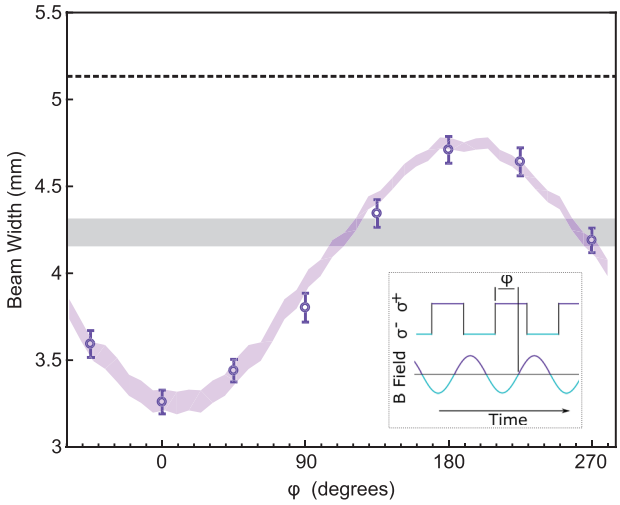

FIG. 4. Molecular beam width as a function of phase offset (φ) between the polarization switching of cooling light and the oscillating magnetic field (see inset). The dashed black line indicates the width of the unperturbed beam, the shaded grey region indicates the measured width and associated error of the Doppler cooled beam without an applied magnetic field, and the shaded purple region indicates Monte Carlo simulation results for the full MO configuration. Clear compression at 0 phase corresponds to the MOT configuration, where the laser polarization provides a spatially confining force. At 180 degrees there is expansion of the beam, corresponding to the anti-MOT configuration. The main cooling light is detuned −7 MHz from resonance while all repumping lasers remain resonant. Error bars represent one standard deviation of the fitted Gaussian beam width.

1.6 mW/cm^2 for the data in Fig. 3 and 3.3 mW/cm^2 for the data in Fig. 4. All data were collected with an rf switching frequency of 530 kHz, a detuning of −7 MHz, and an rf voltage applied to the coils corresponding to a root-mean-square magnetic field gradient of 17 Gauss/cm. Further details on the apparatus are contained in the Supplemental Material [82].

In order to differentiate Doppler and MO effects, we scan the phase of the polarization switching relative to the magnetic field gradient switching, as shown in Fig. 4. The greatest compression of the beam occurs at a phase of 0 degrees and corresponds to the MOT configuration, while at a phase of 180 degrees we see expansion of the beam, corresponding to the anti-MOT. The observed phase dependence is a clear signature of the application of MO forces in addition to the effects of Doppler cooling alone, represented by the gray shaded region in the figure. By measuring the loss of molecules to vibrational dark states as a function of cooling light intensity and by comparing to the known branching ratios of repumped vibrational levels, we are able to determine the number of photons scattered by the cooling process. We find that we can scatter up to 920^{+170}_{-120} photons during the cooling process, limited primarily by interaction time. The beam compression saturates after ~550 photons are scattered. We attribute this saturation to a combination of sub-Doppler heating and MO overfocusing of the molecular beam.

As a means of characterizing our system we use a Monte Carlo simulation to model molecular propagation and cooling dynamics. The MO forces are described by an effective rate-equation model developed previously in diatomic systems [59,86] and described in detail in the Supplemental Material [82]. The resulting forces can be linearized in the form $F_{\mathrm{MO}}/m \approx -\beta v - \omega^2 r$, where m is the molecular mass, r and v are the position and velocity of the molecules, ω is the MO oscillation frequency, and β is the damping constant. By fitting the results of this model to our data we extract MO cooling parameters $\omega \approx 2\pi \times 90$ Hz and $\beta \approx 400$ s^{-1}. These values are comparable to those observed for 2D and 3D MOTs of diatsomic molecules [58,62,64,67]. By fitting the final velocity distribution of the molecular cloud after propagation through the simulated cooling region, we extract transverse beam temperatures. After Doppler cooling alone we find $T = 3.1(1)$ mK (from an initial temperature of $T = 8.4(2)$ mK); with MO cooling and compression the temperature is further reduced to $T = 1.4(1)$ mK. The simulated MOT force is then used to extract an on axis capture velocity of ~7 m/s for a 3D MOT of CaOH, which is similar to that measured in diatomic molecules [63].

In summary, we demonstrate magneto-optical cooling and compression of polyatomic CaOH molecules. We establish a cycling transition and scatter up to ~10^3 photons, limited primarily by interaction time. We also

observe cooling from 8.4 to 1.4 mK. This technique could be used as a means of increasing beam brightness to substantially enhance molecule numbers loaded into a 3D MOT. Demonstrating this degree of photon cycling sets the stage for optical slowing of a molecular beam and ultimately the realization of a full 3D MOT. As a result, this Letter represents a significant step forward in extending cooling and trapping techniques to larger, more complicated molecular species, which will allow the production of ultracold polyatomic molecular samples and deep cooling into the μK regime.

We would like to thank L. Anderegg for insightful discussions. This work was supported by the NSF, AFOSR, and ARO. N. B. V. acknowledges funding from the NDSEG fellowship, and B. L. A. from the NSF GRFP.

*louisbaum@g.harvard.edu

[1] S. Chu, Rev. Mod. Phys. **70**, 685 (1998).
[2] W. D. Phillips, Rev. Mod. Phys. **70**, 721 (1998).
[3] W. Ketterle, Rev. Mod. Phys. **74**, 1131 (2002).
[4] M. D. Swallows, M. Bishof, Y. Lin, S. Blatt, M. J. Martin, A. M. Rey, and J. Ye, Science **331**, 1043 (2011).
[5] I. Bloch, J. Dalibard, and W. Zwerger, Rev. Mod. Phys. **80**, 885 (2008).
[6] L. D. Carr, D. DeMille, R. V. Krems, and J. Ye, New J. Phys. **11**, 055049 (2009).
[7] J. Baron, W. C. Campbell, D. DeMille, J. M. Doyle, G. Gabrielse, Y. V. Gurevich, P. W. Hess, N. R. Hutzler, E. Kirilov, I. Kozyryev *et al.*, Science **343**, 269 (2014).
[8] V. Andreev and N. R. Hutzler, Nature (London) **562**, 355 (2018).
[9] J. J. Hudson, B. E. Sauer, M. R. Tarbutt, and E. A. Hinds, Phys. Rev. Lett. **89**, 023003 (2002).
[10] W. B. Cairncross, D. N. Gresh, M. Grau, K. C. Cossel, T. S. Roussy, Y. Ni, Y. Zhou, J. Ye, and E. A. Cornell, Phys. Rev. Lett. **119**, 153001 (2017).
[11] A. Micheli, G. Brennen, and P. Zoller, Nat. Phys. **2**, 341 (2006).
[12] S. R. Manmana, E. M. Stoudenmire, K. R. A. Hazzard, A. M. Rey, and A. V. Gorshkov, Phys. Rev. B **87**, 081106(R) (2013).
[13] L. Anderegg, L. W. Cheuk, Y. Bao, S. Burchesky, W. Ketterle, K.-K. Ni, and J. M. Doyle, Science **365**, 1156 (2019).
[14] Y. Segev, M. Pitzer, M. Karpov, N. Akerman, J. Narevicius, and E. Narevicius, Nature (London) **572**, 189 (2019).
[15] J. L. Bohn, A. M. Rey, and J. Ye, Science **357**, 1002 (2017).
[16] S. Ospelkaus, K.-K. Ni, D. Wang, M. De Miranda, B. Neyenhuis, G. Quéméner, P. Julienne, J. Bohn, D. Jin, and J. Ye, Science **327**, 853 (2010).
[17] M.-G. Hu, Y. Liu, D. D. Grimes, Y.-W. Lin, A. H. Gheorghe, R. Vexiau, N. Bouloufa-Maafa, O. Dulieu, T. Rosenband, and K.-K. Ni, Science **366**, 1111 (2019).
[18] I. C. Lane, Phys. Chem. Chem. Phys. **14**, 15078 (2012).
[19] N. Wells and I. C. Lane, Phys. Chem. Chem. Phys. **13**, 19036 (2011).
[20] I. Kozyryev and N. R. Hutzler, Phys. Rev. Lett. **119**, 133002 (2017).
[21] I. Kozyryev, Z. Lasner, and J. M. Doyle, arXiv:1805.08185.
[22] C. M. Tesch and R. de Vivie-Riedle, Phys. Rev. Lett. **89**, 157901 (2002).
[23] Q. Wei, S. Kais, B. Friedrich, and D. Herschbach, J. Chem. Phys. **135**, 154102 (2011).
[24] P. Yu, L. W. Cheuk, I. Kozyryev, and J. M. Doyle, New J. Phys. **21**, 093049 (2019).
[25] M. Wall, K. Maeda, and L. D. Carr, New J. Phys. **17**, 025001 (2015).
[26] M. L. Wall, K. Maeda, and L. D. Carr, Ann. Phys. (Berlin) **525**, 845 (2013).
[27] A. Lazcano and S. L. Miller, Cell **85**, 793 (1996).
[28] M. Quack, Angew. Chem. **28**, 571 (1989).
[29] M. Quack, Angew. Chem. **41**, 4618 (2002).
[30] L. D. Augustovičová and J. L. Bohn, New J. Phys. **21**, 103022 (2019).
[31] R. V. Krems, *Molecules in Electromagnetic Fields* (John Wiley & Sons, Hoboken, NJ, 2018).
[32] L. De Marco, G. Valtolina, K. Matsuda, W. G. Tobias, J. P. Covey, and J. Ye, Science **363**, 853 (2019).
[33] K.-K. Ni, S. Ospelkaus, M. H. G. de Miranda, A. Pe'er, B. Neyenhuis, J. J. Zirbel, S. Kotochigova, P. S. Julienne, D. S. Jin, and J. Ye, Science **322**, 231 (2008).
[34] R. Fulton, A. I. Bishop, and P. F. Barker, Phys. Rev. Lett. **93**, 243004 (2004).
[35] E. Lavert-Ofir, S. Gersten, A. B. Henson, I. Shani, L. David, J. Narevicius, and E. Narevicius, New J. Phys. **13**, 103030 (2011).
[36] X. Wu, T. Gantner, M. Koller, M. Zeppenfeld, S. Chervenkov, and G. Rempe, Science **358**, 645 (2017).
[37] N. Vanhaecke, U. Meier, M. Andrist, B. H. Meier, and F. Merkt, Phys. Rev. A **75**, 031402 (2007).
[38] Y. Liu, M. Vashishta, P. Djuricanin, S. Zhou, W. Zhong, T. Mittertreiner, D. Carty, and T. Momose, Phys. Rev. Lett. **118**, 093201 (2017).
[39] N. Fitch and M. Tarbutt, Chem. Phys. Chem. **17**, 3609 (2016).
[40] M. Petzold, P. Kaebert, P. Gersema, M. Siercke, and S. Ospelkaus, New J. Phys. **20**, 042001 (2018).
[41] E. S. Shuman, J. F. Barry, D. R. Glenn, and D. DeMille, Phys. Rev. Lett. **103**, 223001 (2009).
[42] B. Hemmerling, E. Chae, A. Ravi, L. Anderegg, G. K. Drayna, N. R. Hutzler, A. L. Collopy, J. Ye, W. Ketterle, and J. M. Doyle, J. Phys. B **49**, 174001 (2016).
[43] M. Zeppenfeld, B. G. Englert, R. Glöckner, A. Prehn, M. Mielenz, C. Sommer, L. D. van Buuren, M. Motsch, and G. Rempe, Nature (London) **491**, 570 (2012).
[44] A. Prehn, M. Ibrügger, R. Glöckner, G. Rempe, and M. Zeppenfeld, Phys. Rev. Lett. **116**, 063005 (2016).
[45] B. K. Stuhl, B. C. Sawyer, D. Wang, and J. Ye, Phys. Rev. Lett. **101**, 243002 (2008).
[46] M. Di Rosa, Eur. Phys. J. D **31**, 395 (2004).
[47] D. McCarron, J. Phys. B **51**, 212001 (2018).
[48] M. Tarbutt, Contemp. Phys. **59**, 356 (2018).
[49] J. Lim, J. R. Almond, M. A. Trigatzis, J. A. Devlin, N. Fitch, B. Sauer, M. Tarbutt, and E. Hinds, Phys. Rev. Lett. **120**, 123201 (2018).

[50] S. Truppe, S. Marx, S. Kray, M. Doppelbauer, S. Hofsäss, H. C. Schewe, N. Walter, J. Pérez-Ríos, B. G. Sartakov, and G. Meijer, Phys. Rev. A **100**, 052513 (2019).

[51] N. Wells and I. C. Lane, Phys. Chem. Chem. Phys. **13**, 19018 (2011).

[52] I. Kozyryev, L. Baum, K. Matsuda, and J. M. Doyle, Chem. Phys. Chem. **17**, 3641 (2016).

[53] M. V. Ivanov, S. Gulania, and A. I. Krylov, J. Phys. Chem. Lett. **11**, 1297 (2020).

[54] J. Kłos and S. Kotochigova, arXiv:1912.09364.

[55] E. S. Shuman, J. F. Barry, and D. DeMille, Nature (London) **467**, 820 (2010).

[56] J. F. Barry, E. S. Shuman, E. B. Norrgard, and D. DeMille, Phys. Rev. Lett. **108**, 103002 (2012).

[57] J. F. Barry, D. McCarron, E. Norrgard, M. Steinecker, and D. DeMille, Nature (London) **512**, 286 (2014).

[58] D. McCarron, E. Norrgard, M. Steinecker, and D. DeMille, New J. Phys. **17**, 035014 (2015).

[59] E. B. Norrgard, D. J. McCarron, M. H. Steinecker, M. R. Tarbutt, and D. DeMille, Phys. Rev. Lett. **116**, 063004 (2016).

[60] M. H. Steinecker, D. J. McCarron, Y. Zhu, and D. DeMille, Chem. Phys. Chem. **17**, 3664 (2016).

[61] E. Chae, L. Anderegg, B. L. Augenbraun, A. Ravi, B. Hemmerling, N. R. Hutzler, A. L. Collopy, J. Ye, W. Ketterle, and J. M. Doyle, New J. Phys. **19**, 033035 (2017).

[62] L. Anderegg, B. L. Augenbraun, E. Chae, B. Hemmerling, N. R. Hutzler, A. Ravi, A. Collopy, J. Ye, W. Ketterle, and J. M. Doyle, Phys. Rev. Lett. **119**, 103201 (2017).

[63] H. Williams, S. Truppe, M. Hambach, L. Caldwell, N. Fitch, E. Hinds, B. Sauer, and M. Tarbutt, New J. Phys. **19**, 113035 (2017).

[64] S. Truppe, H. Williams, M. Hambach, L. Caldwell, N. Fitch, E. Hinds, B. Sauer, and M. Tarbutt, Nat. Phys. **13**, 1173 (2017).

[65] S. Truppe, H. Williams, N. Fitch, M. Hambach, T. Wall, E. Hinds, B. Sauer, and M. Tarbutt, New J. Phys. **19**, 022001 (2017).

[66] L. Caldwell, J. A. Devlin, H. J. Williams, N. J. Fitch, E. A. Hinds, B. E. Sauer, and M. R. Tarbutt, Phys. Rev. Lett. **123**, 033202 (2019).

[67] M. T. Hummon, M. Yeo, B. K. Stuhl, A. L. Collopy, Y. Xia, and J. Ye, Phys. Rev. Lett. **110**, 143001 (2013).

[68] M. Yeo, M. T. Hummon, A. L. Collopy, B. Yan, B. Hemmerling, E. Chae, J. M. Doyle, and J. Ye, Phys. Rev. Lett. **114**, 223003 (2015).

[69] A. L. Collopy, S. Ding, Y. Wu, I. A. Finneran, L. Anderegg, B. L. Augenbraun, J. M. Doyle, and J. Ye, Phys. Rev. Lett. **121**, 213201 (2018).

[70] L. Anderegg, B. L. Augenbraun, Y. Bao, S. Burchesky, L. W. Cheuk, W. Ketterle, and J. M. Doyle, Nat. Phys. **14**, 890 (2018).

[71] D. J. McCarron, M. H. Steinecker, Y. Zhu, and D. DeMille, Phys. Rev. Lett. **121**, 013202 (2018).

[72] H. J. Williams, L. Caldwell, N. J. Fitch, S. Truppe, J. Rodewald, E. A. Hinds, B. E. Sauer, and M. R. Tarbutt, Phys. Rev. Lett. **120**, 163201 (2018).

[73] I. Kozyryev, L. Baum, K. Matsuda, B. L. Augenbraun, L. Anderegg, A. P. Sedlack, and J. M. Doyle, Phys. Rev. Lett. **118**, 173201 (2017).

[74] B. L. Augenbraun, Z. D. Lasner, A. Frenett, H. Sawaoka, C. Miller, T. C. Steimle, and J. M. Doyle, New J. Phys. (2020).

[75] I. Kozyryev, L. Baum, L. Aldridge, P. Yu, E. E. Eyler, and J. M. Doyle, Phys. Rev. Lett. **120**, 063205 (2018).

[76] I. Kozyryev, T. C. Steimle, P. Yu, D.-T. Nguyen, and J. M. Doyle, New J. Phys. **21**, 052002 (2019).

[77] D. Trung (private communication).

[78] G. Herzberg, *Molecular Spectra and Molecular Structure. Vol. 3* (Van Nostrand Reinhold, New York, 1966).

[79] C. Scurlock, D. Fletcher, and T. Steimle, J. Mol. Spectrosc. **159**, 350 (1993).

[80] C. Brazier and P. Bernath, J. Mol. Spectrosc. **114**, 163 (1985).

[81] E. Hirota, *High-Resolution Spectroscopy of Transient Molecules* (Springer-Verlag, Berlin, 1985).

[82] See the Supplemental Material at http://link.aps.org/supplemental/10.1103/PhysRevLett.124.133201 for additional information on vibrational branching ratios and details of the Monte Carlo simulation.

[83] M. Tarbutt, New J. Phys. **17**, 015007 (2015).

[84] N. R. Hutzler, H.-I. Lu, and J. M. Doyle, Chem. Rev. **112**, 4803 (2012).

[85] J. F. Barry, E. Shuman, and D. DeMille, Phys. Chem. Chem. Phys. **13**, 18936 (2011).

[86] M. R. Tarbutt, B. E. Sauer, J. J. Hudson, and E. A. Hinds, New J. Phys. **15**, 053034 (2013).